PROCEEDINGS, Thirty-Seventh Workshop on Geothermal Reservoir Engineering
Stanford University, Stanford, California, January 30 - February 1, 2012
SGP-TR-194

CHARACTERIZATION OF FRACTURES IN GEOTHERMAL RESERVOIRS USING RESISTIVITY

Lilja Magnusdottir and Roland Horne

Stanford University, Department of Energy Resources Engineering
367 Panama Street
Stanford, CA 94305-2220, USA
e-mail: liljam@stanford.edu

ABSTRACT

This paper describes a method to provide information about fracture topology in geothermal reservoirs using Electrical Resistivity Tomography (ERT). Fracture characterization in Enhanced Geothermal Systems (EGS) is crucial to ensure adequate supply of geothermal fluids and efficient thermal operation of the wells. The knowledge of fluid-flow patterns in the reservoir helps preventing short-circuiting flow paths from injector to producer that would lead to premature thermal breakthrough.

The resistivity distribution of a field can be estimated by measuring potential differences between various points while injecting an electric current into the ground, and resistivity data can be used to infer fracture properties due to the large contrast in resistivity between water and rock. The inverse method requires a large parameter space and can be hard to solve so it is important to find ways to improve the fracture characterization process. In this study, the contrast between rock and fractures was enhanced by injecting a conductive tracer into the reservoir, thereby decreasing the resistivity of the fractures as the fluid flows through the fracture network. The time history of the potential difference between two points (an injector and a producer), which corresponds to the resistivity changes, depends on the fracture network and therefore helps estimate where fractures are located and the character of their distribution.

The flow simulator TOUGH2 was used to calculate how the conductive tracer distributes through the reservoir and the analogy between Ohm's law that describes electrical flow and Darcy's law describing fluid flow made it possible to use TOUGH2 also to calculate the electric fields. The EOS1 module in TOUGH2 was used to calculate the tracer flow and EOS9 module was used to calculate the electric potential. First, the electric potential calculated using the ESO9 module was verified by comparing the results to an analytical solution. Next, the time history of the potential difference between an injector and a producer was calculated for two simple fracture networks to explore the relationship between fracture networks and the changes in potential field.

The time histories of the potential difference was also studied for more realistic fracture networks by using a discrete-fracture model introduced by Karimi-Fard et al. (2003) to create more complicated fracture networks. The method used is based on an unstructured control volume finite-difference formulation where the cell connections are defined using a connectivity list. Four cases were studied and they all gave different results for the time histories of the potential difference, verifying that the potential field is dependent on the fracture networks. By studying this relationship further the changes in potential fields could be used to provide information about the fractures characteristics.

INTRODUCTION

Electrical Resistivity Tomography (ERT) is a technique used to image the subsurface using electrical measurements made through electrodes at the surface. The method is similar to Electrical Impedance Tomography (EIT) used in the medical industry to image the internal conductivity of the human body, for example to monitor epilepsy, strokes and lung functions, as discussed by Holder (2004). Based on a theoretical study, Pritchett (2004) concluded that hidden geothermal resources can be explored by electrical resistivity measurements because the electrical current moving through the reservoir passes mainly through fluid-filled fractures and pore spaces. Geothermal reservoirs can therefore be characterized by substantially reduced electrical resistivity relative to their surroundings.

Slater et al. (2000) have shown a possible way of using ERT with a tracer injection by observing tracer

migration through a sand/clay sequence in an experimental 10 × 10 × 3 m^3 tank with cross-borehole electrical imaging. Singha and Gorelick (2005) also used cross-well electrical imaging to monitor migration of a saline tracer in a 10 × 14 × 35 m^3 tank. In previous work, usually many electrodes were used to obtain the resistivity distribution for the whole field at each time step. The resistivity distribution was then compared to the background distribution (without any tracer) to see resistivity changes in each block visually. These resistivity changes helped locate the saline tracer and thereby the fractures. Using this method for a whole reservoir would require a gigantic parameter space, and the inverse problem would not likely be solvable, except at very low resolution. However, in the method considered in this study, the potential difference between the wells which corresponds to the changes in resistivity, would be measured and plotted as a function of time while the conductive tracer flows through the fracture network. Future work will involve finding ways to use that response, i.e. potential difference vs. time, in an inverse modeling process to help characterizing the fracture pattern.

FLOW SIMULATOR TOUGH2 USED TO SOLVE THE ELECTRIC FIELD

The potential distribution in steady state porous flow is exactly the same as the potential distribution in an electric conducting medium due to the analogy between Darcy's law and Ohm's law, as formulated by Muskat (1932). Therefore, flow simulator TOUGH2 can be used to calculate both the distribution of a conductive tracer in the reservoir as well as to solve the electric field at each time step. The same grid can then be used for both electric and fluid flow models, making the simulation more efficient than if separate models were used.

Water Flow Analogy of Electrical Flow

Darcy's law is an empirical relationship similar to Ohm's law,

$$J = -\sigma \nabla \varphi \qquad (1)$$

where J is current density [A/m^2], σ is the conductivity of the medium [Ωm] and φ is the electric potential [V], but instead of describing electrical flow Darcy's law describes fluid flow through a porous medium,

$$q = -\frac{k}{\mu} \nabla p \qquad (2)$$

where q is the flow rate [m/s], k is permeability [m^2], μ is viscosity of the fluid [kg/ms] and p is pressure [Pa]. Table 1 presents the correspondence between the variables and relations of water flow (Darcy's law) and electric current flow (Ohm's law).

Table 1: Correspondence between electric current flow and water flow.

	Darcy's law:	Ohm's law:
Flux of:	Water q [m/s]	Charge J [A/m^3]
Potential:	Pressure p [Pa]	Voltage φ [V]
Medium property:	Hydraulic conductivity $\frac{k}{\mu}$ [m^2/Pa·s]	Electrical conductivity σ [1/Ωm]

The similarities between these two equations imply that it is possible to use a flow simulator like TOUGH2 to solve the electric field due to flow of electric current. The pressure results from TOUGH2 correspond to the electric voltage, the current density to the flow of water and the electrical conductivity corresponds to the hydraulic conductivity, i.e.

$$\sigma = \frac{k}{\mu} \qquad (3)$$

However, it must be taken into account that viscosity depends on pressure while conductivity of a reservoir does not depend on the electric voltage used. Figure 1 shows how viscosity of water at 150°C changes with pressure.

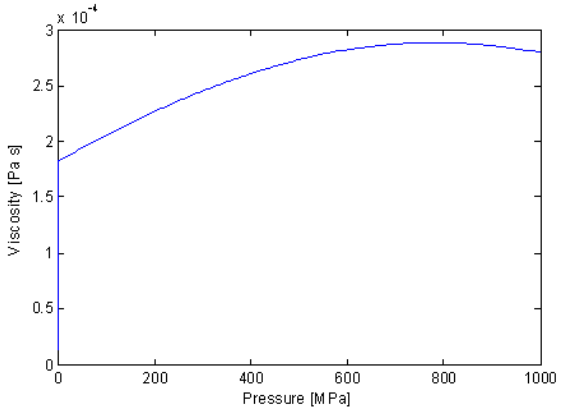

Figure 1: Viscosity [Pa·s] as a function of pressure [MPa].

In order to take the pressure dependence into account, the EOS9 module in TOUGH2 was studied. EOS9 considers flow of a single aqueous phase consisting of a single water component. The conditions are

assumed to be isothermal so only a single water mass balance equation is solved for each grid block and the thermal properties of water can be overwritten. Therefore, liquid viscosity, density and compressibility can be defined constant and reference pressure and temperature can be overwritten, making the imitation of electric flow possible.

EOS9 results compared to the analytical solution

The electric field was calculated for a 3 × 3 block matrix using EOS9 with density and viscosity defined constant and the flow simulation parameters defined as previously described. The simulation was carried out on an inhomogeneous two-dimensional grid with dimensions 10 × 10 × 1 m^3, see Figure 2, and the results were compared to the analytical solution.

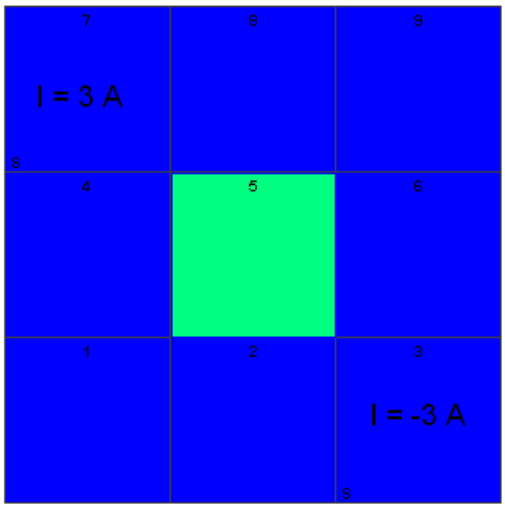

Figure 2: Inhomogeneous electric model with the current set as 3 A in the upper left corner and as -3 A in the lower right corner.

The resistivity of the middle block (green) was set as 0.0025 Ωm and the resistivity of the other blocks (blue) was set as 0.005 Ωm. The electric current was modeled to be 3 A in the upper left corner and -3 A in the lower right corner, and the initial electric potential was set as zero.

The pressure solved in a flow simulation is usually of higher magnitude than the voltage in the electric case. Therefore, in order to solve the electric problem using a flow simulator, some of the electric parameters need to be scaled. The initial pressure is set to 10^6 Pa and the injection to $\pm 3 \times 10^8$ kg/s, so the appropriate pressure has to be subtracted from the pressure results in order to obtain the electric potential results assuming initial voltage to be zero. The results are then multiplied by 10^2 to get the electric potential results in volts.

The results from EOS9 module were compared to the analytical solution calculated using the following equation, as described in Magnusdottir and Horne (2010).

$$\varphi(j,k) = \frac{\begin{bmatrix} Ihl + \varphi(j+1,k)c_1 l^2 + \varphi(j-1,k)c_2 l^2 \\ + \varphi(j,k+1)c_3 h^2 + \varphi(j,k-1)c_4 h^2 \end{bmatrix}}{[c_1 + c_2]l^2 + [c_3 + c_4]h^2} \quad (4)$$

The parameter φ is the electric potential [*V*], parameters c_i represent the conductivity averaged (harmonic average) between two adjacent blocks, *I* [amp] is the current injected at point (*j*,*k*) and h is the height of the block and *l* is the length [m].

The EOS9 solution was the same as the analytical solution, see Table 2. The rows of the tables represent the rows of blocks shown in Figure 2.

Table 2: Electric potential calculated using EOS9 module in TOUGH2, which is equal to the analytical solution.

0.0107 V	*0.0032 V*	*0 V*
0.0032 V	*0 V*	*-0.0032 V*
0 V	*-0.0032 V*	*-0.0107 V*

Therefore, the EOS9 module in TOUGH2 has successfully been used to calculate the electric field for an inhomogeneous case by defining the water density, viscosity and compressibility constant.

Two simple fracture networks studied

Flow simulations were performed using the EOS1 module in TOUGH2 reservoir simulator to see how a tracer, which increases the conductivity of the fluid, distributes after being injected into different reservoirs. The simulations were carried out on two-dimensional grids with dimensions 2000 × 2000 × 1 m^3 with fractures first modeled as a long path from the injector to the producer as shown in Figure 3 and then as a path straight from the injector to the producer, shown in Figure 4. The goal was to study the difference in potential field history between these two cases as conductive fluid is injected into the reservoir.

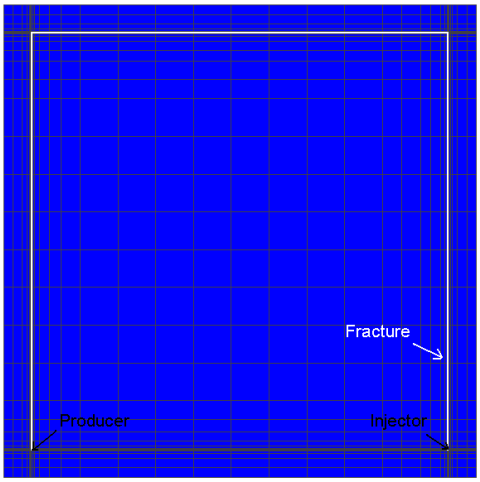

Figure 3: Reservoir with a fracture from the injector, around the reservoir and to the producer.

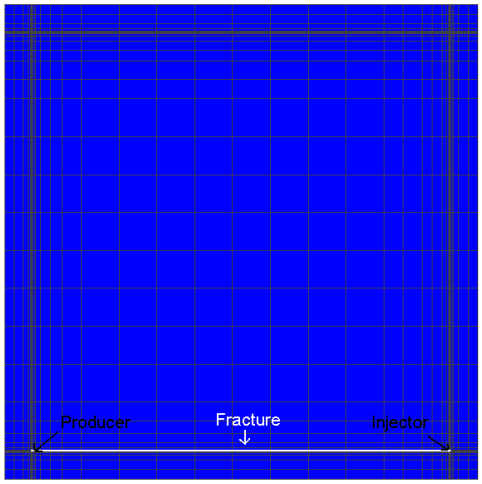

Figure 4: Reservoir with a fracture straight from the injector to the producer.

The reservoir is modeled with a porosity of 0.2 and a permeability of 10^6 md (10^{-9} m^2) while the fractures have a permeability of 10^{11} md (10^{-4} m^2). No-flow boundary conditions were used and 100 kg/s of water was injected in the lower right corner with enthalpy 100 kJ/kg, and 0.1 kg/s of tracer with enthalpy 100 kJ/kg. The initial pressure was set to 10^6 Pa, temperature to 150°C and initial tracer mass fraction to 10^{-9} because the simulator could not solve the problem with a zero initial tracer mass fraction.

The tracer injected into the reservoir is a NaCl solution whose resistivity changes with temperature and concentration. Ucok et al. (1980) have established experimentally the resistivity of saline fluids over the temperature range 20-350°C and their results for resistivity of NaCl solution calculated using a three-dimensional regression formula is shown in Figure 5.

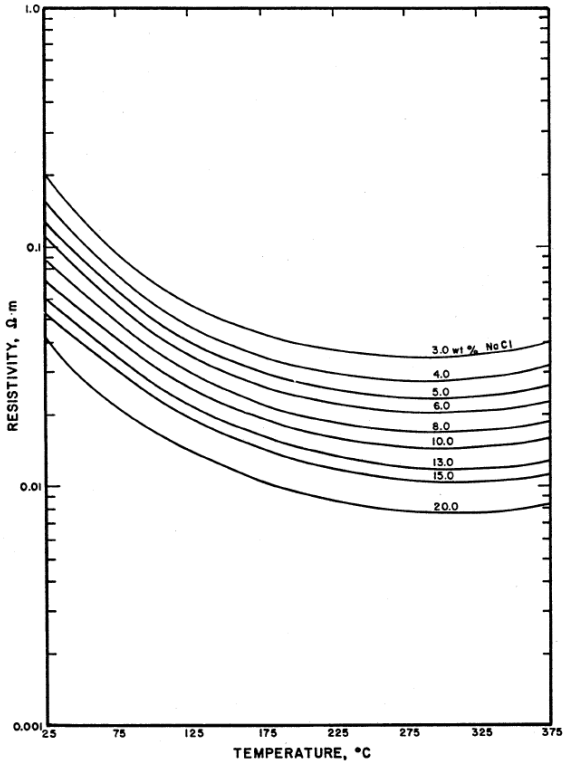

Figure 5: Resistivity of NaCl solution as a function of temperature and concentration (Ucok et al., 1980).

Ucok et al. (1980) calculated that the dependence of resistivity is best represented by the formula:

$$\rho_w = b_0 + b_1 T^{-1} + b_2 T + b_3 T^2 + b_4 T^3 \quad (5)$$

where T is temperature and b are coefficients found empirically. The best fit for the concentration dependence was found to be:

$$\rho_w = 10/(\Lambda c) \quad (6)$$

where

$$\Lambda = B_0 - B_1 c^{1/2} + B_2 c \ln c + higher\ order\ terms \quad (7)$$

Coefficients B depend on the solution chemistry and c is the molar concentration.

In this project, the tracer concentration resulting from the flow simulation is changed into molar concentration and the following B coefficient matrix for the three-dimensional regression analysis of the data studied by Ucok et al. (1980) is used to calculate the resistivity of the NaCl solution,

$$B = \begin{matrix} 3.470 & -6.650 & 2.633 \\ -59.23 & 198.1 & 64.80 \\ 0.4551 & -0.2058 & 0.005799 \\ -0.346E\text{-}5 & 7.368E\text{-}5 & 6.741E\text{-}5 \\ -1.766E\text{-}6 & 8.787E\text{-}7 & -2.136E\text{-}7 \end{matrix}$$

Then, the resistivity of water saturated rock, ρ, is calculated using Archie's law,

$$\rho = a\emptyset^{-b}\rho_w \qquad (8)$$

where ϕ is the porosity of the rock and a and b are empirical constants, here a is set as 1 and b as 2. The resistivity value of each block, therefore depends on the tracer concentration in that block and the value decreases as more tracer flows into the block.

The EOS9 module in TOUGH2 was used to calculate the electric potential distribution for the reservoirs in Figures 3 and 4. A current was set equal to 1 A at the injector and as -1 A at the producer and the potential field calculated based on the resistivity of the field at each time step. Figures 6 shows how the potential difference, which corresponds to the changes in resistivity, between the injector and the producer changes with time for the reservoirs in Figure 3 and Figure 4.

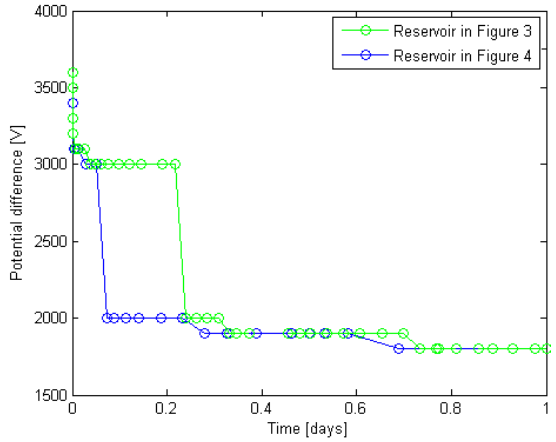

Figure 6: Potential difference between wells for reservoirs in Figure 3 and Figure 4.

Figure 6 clearly illustrates that the electric potential history is different for the two fracture networks. After 0.239 days the potential difference plotted in green (reservoir in Figure 3) drops from 3000 V to 2000 V but the potential difference plotted in blue (reservoir in Figure 4) drops the same amount much earlier, or after 0.074 days. Therefore, these histories of the potential differences show that the conductive tracer flows faster through the fracture network in Figure 4 than in Figure 3 which tells us that the fracture path from the injector to the producer is shorter for that fracture network. In these examples, as well as in all following examples, it is assumed that the reservoir does not have any water until the conductive water is injected into the reservoir. The resistivity between the injector and the producer is therefore very high until the tracer reaches the production well, allowing the current to flow easily between the wells. When the tracer has gone fully through the fracture networks for both cases the potential differences are the same.

These results show that the potential difference histories with conductive tracer flow give valuable information about the fracture networks and can therefore help characterize the fractures.

DISCRETE FRACTURE NETWORKS

Discrete Fracture Network (DFN) models represent fracture-dominated flow paths in geothermal reservoirs more accurately since the fractures are treated discretely instead of being defined by high permeability values in course-scale grid blocks, as done in the previous example. By employing a DFN approach introduced by Karimi-Fard et al. (2003) we were able to generate a more realistic fracture network with fracture grid blocks of realistic dimensions. A MATLAB code written by Juliusson and Horne (2009) was used to generate a two-dimensional stochastic fracture network, run flow simulations on the network with TOUGH2, and plot the tracer flow results. EOS1 module in TOUGH2 was used to both solve the tracer flow as well as the electric flow. Figure 7 shows the fracture network generated, where the computational grid was formed using the triangular mesh generator Triangle, developed by Shewchuk (1996).

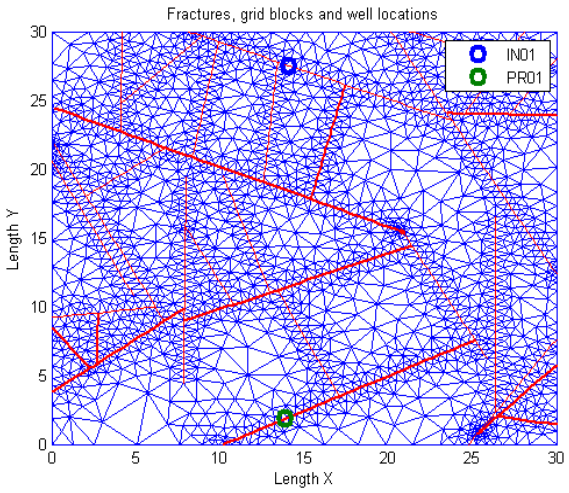

Figure 7: Two-dimensional discrete fracture network.

The dimensions of the two-dimensional grid were 30 × 30 × 1 m^2 and closed (no-flow) boundary conditions were used. The porosity of the fractures was set to 0.9 and the width, w, was assigned as a function of the fracture length L,

$$w = L \cdot 10^{-2} \quad (9)$$

The corresponding permeability was determined by

$$k = \frac{w^2}{2\,4} \quad (10)$$

The matrix blocks were given a porosity value of 0.12 and a very low permeability value so the conductive fluid only flows through the fractures.

By using the DFN approach every element (both triangles and fracture segments) was given a transmissibility value which is related to the flow between two adjoining elements as,

$$Q_{ij} = T_{ij}(p_j - p_i) \quad (11)$$

where Q is the flow rate between gridblocks i and j, T is the transmissibility and p is the pressure. More details on the approach can be found in the reference by Karimi-Fard et al. (2003).

Case 1

The well configuration for Case 1 is shown in Figure 7, an injection well at the top of the figure and a production well at the bottom. Water was injected at the rate of 5.6 × 10^{-2} kg/s with enthalpy 3.14 × 10^5 kJ/kg and the tracer injected was 0.1% of the water injected. The production well was modeled to deliver against a bottomhole pressure of 10^6 Pa with productivity index of 4 × 10^{-12} m^3 (as specified for TOUGH2). The initial pressure was set to 10^6 Pa and the temperature to 25°C and the initial tracer mass fraction was set to 10^{-7} kg_{tracer}/kg_{total} because TOUGH2 could not to solve the problem with initial tracer set as zero.

Figure 8 shows how the tracer concentration in the producer (green) changed with time as more tracer was injected into the reservoir.

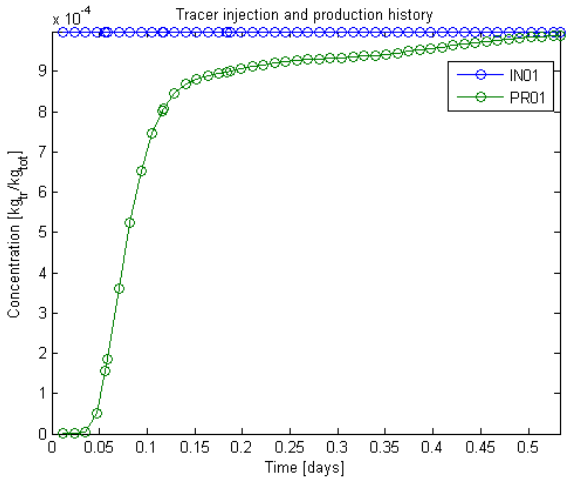

Figure 8: Tracer history at the injector and at the producer.

The electrical resistivity method described earlier was used to examine how the potential difference history, which corresponds to the changes in resistivity, relates to the fracture network. The current was set as 1 A at the injector and as -1 A at the producer and the potential field calculated. The potential difference between the injector and the producer drops very fast to begin with, as tracer is being injected, see Figure 9.

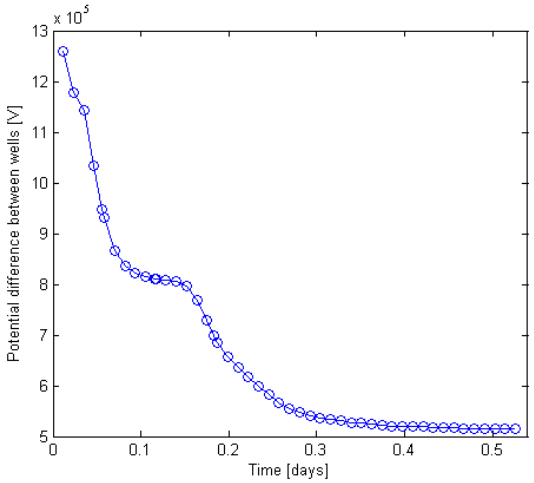

Figure 9: Potential difference between the injector and the producer.

After about 0.08 days the potential difference starts decreasing more slowly until after approximately 0.15 days where it drops relatively faster until it reaches about 52 V. Figures 10 shows the tracer distribution after approximately 0.01, 0.08, 0.15 and 0.35 days.

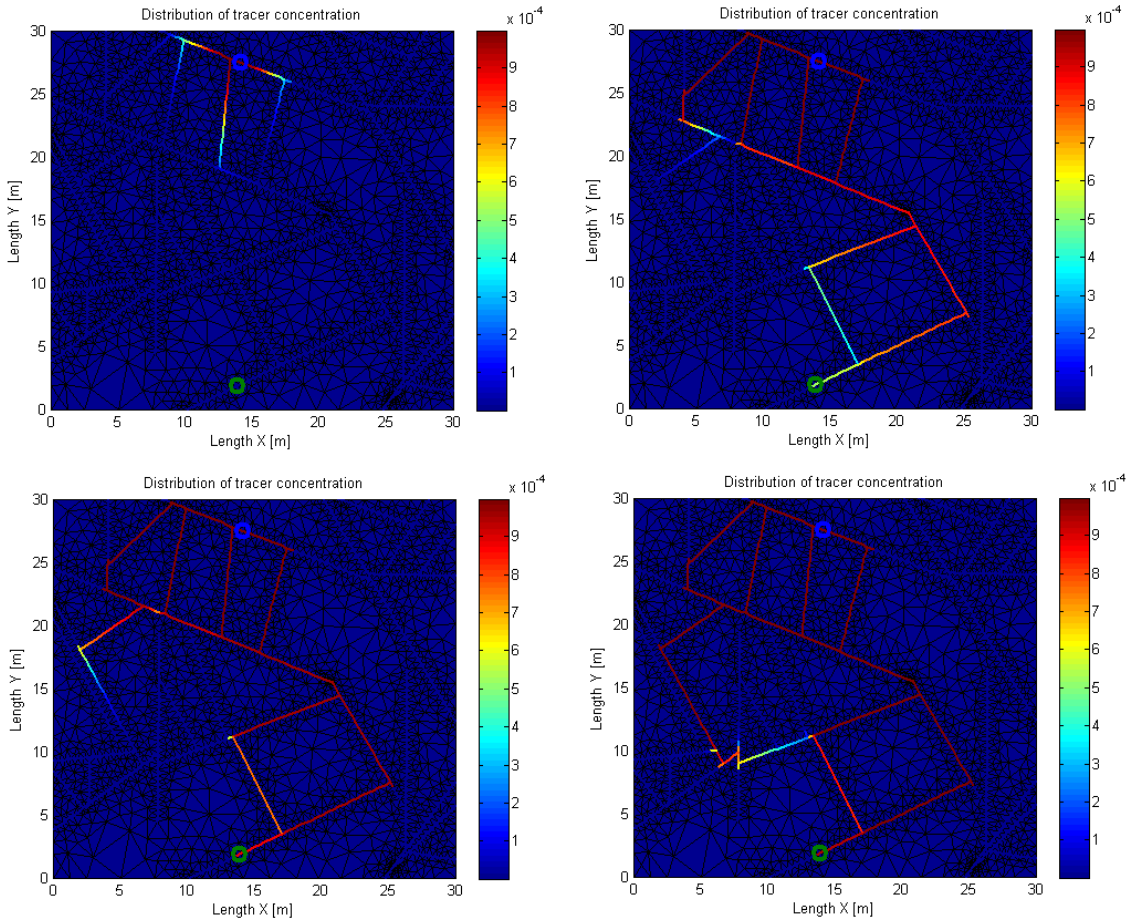

Figure 10: Tracer distribution in the reservoir after 0.01 days (upper left corner), 0.08 days (upper right corner), 0.15 days (lower left corner) and after 0.35 days (lower right corner).

By examining the tracer flow it can be seen that the potential difference starts decreasing more slowly as the tracer has reached the production well. As the reservoir has a very high resistivity until the tracer flows through the fractures it can be thought of as an electric circuit where in the lower left corner of Figure 10 the resistance is very high except for the formed path (in red) from the injector to the producer. Once these fractures have been filled the potential difference stops decreasing as much because the current will flow through the previously formed path until another path has been fully formed. When another path to the left has been formed, the 'circuit' has two paths connected in parallel, see lower right corner of Figure 10. Therefore, the potential difference starts dropping again until the second path to the left has also been fully concentrated with tracer. Once the tracer has entirely reached the producer from all possible fracture paths the potential difference stops decreasing.

Case 2

For the second case, the locations of the injector and the producer were switched. Now, after about 0.01 days the tracer flow has only been divided into two flow paths, see Figure 11, instead of three paths as for Case 1 (shown in the upper left part of Figure 10).

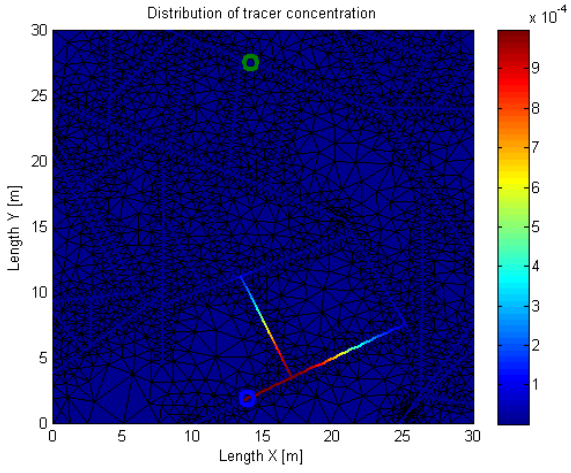

Figure 11: Tracer distribution in the reservoir for Case 2 after 0.01 days of tracer injection.

Therefore, the tracer in Case 2 is being distributed faster towards the producer which results in the potential difference dropping a little bit faster, as can be seen in Figure 12 where the potential difference time histories for Case 1 and Case 2 are compared.

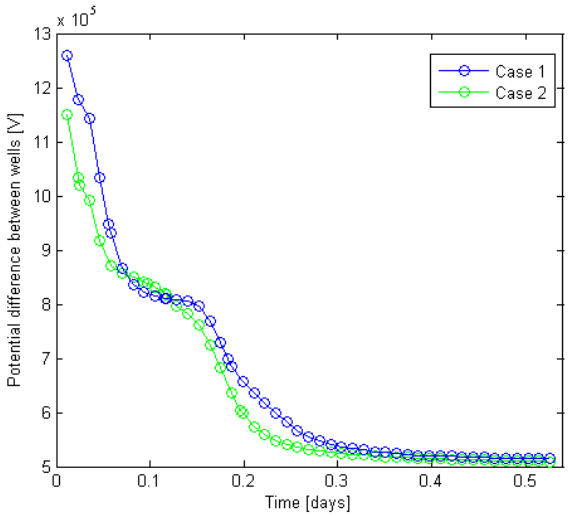

Figure 12: Time histories of potential differences for Case 1 and Case 2.

The potential fields are somewhat different for these two cases because the flow paths are different until the tracer has reached the production well through all possible fracture paths for both cases.

Case 3

In the third case, the injection well and the production well were located closer to each other, see Figure 13, to investigate whether the resistivity (or the potential difference) decreases faster than in previous cases.

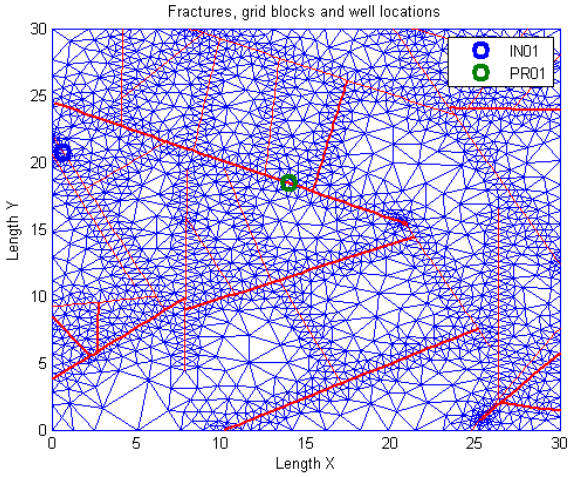

Figure 13: Two-dimensional discrete fracture network with the injector and the producer located close to each other.

The tracer distributes faster from the injection well to the production well than for Case 1, as can be seen by comparing Figure 14 to Figure 8, since the wells are connected and located closer to each other.

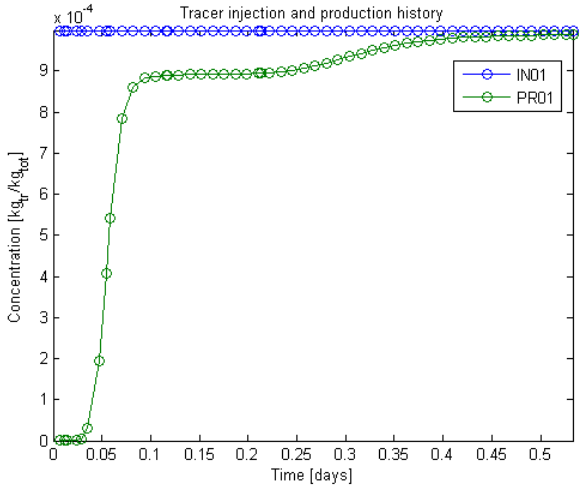

Figure 14: Tracer history at the injector and at the producer for Case 3.

After 0.09 days the tracer concentration at the producer has reached 8.8×10^{-4}, compared to only about 6×10^{-4} for Case 1 (see Figure 8). Figure 15 shows the potential difference for Case 3 as well as for Case 1.

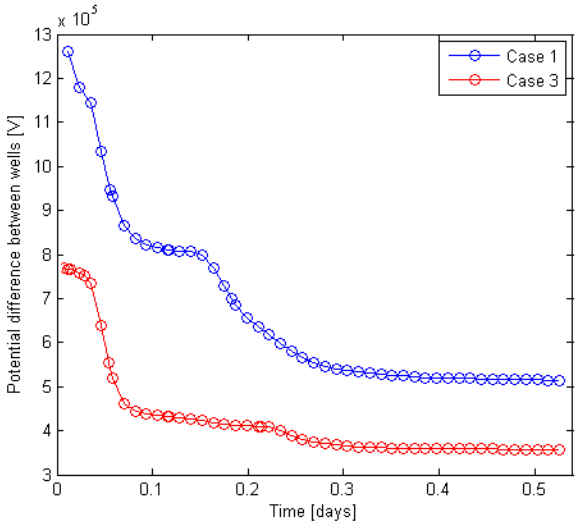

Figure 15: Time histories of potential differences for Case 1 and Case 3.

The potential difference is less for Case 3 since there is less distance between the wells and it has dropped all the way down to 4×10^5 V after only 0.08 days, which is close to the steady state difference, 3.6×10^5 V. Most of the current will go through the first path formed from the injector to the producer, even once another path has been formed because the

second path is considerably longer than the first path. Therefore, the potential difference only drops slightly once the second path is formed. In Case 1, the potential difference has only dropped down to 8.4×10^5 V after 0.08 days but it drops down to 5.2×10^5 V once the second path is formed since in that case similar amount of current will be flowing through the two different paths. The shapes of the two curves are therefore distinctive, since each one corresponds to its flow path, i.e. its fracture network.

Case 4

By increasing the number of wells more information can be provided and used to distinguish between possible fracture patterns. In Case 4, one injection well was modeled and two production wells, see well configuration in Figure 16.

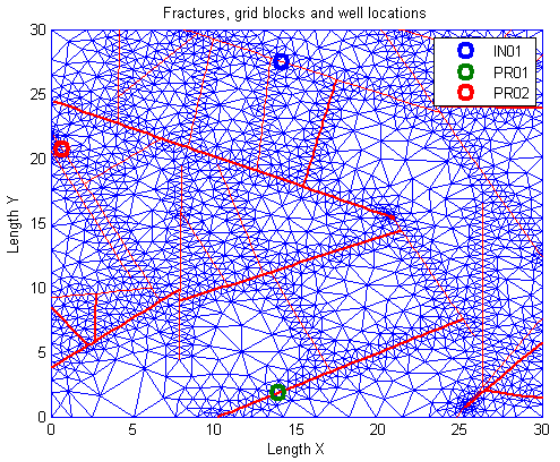

Figure 16: Two-dimensional discrete fracture network with one injector and two producers.

The injection was the same as for previous cases but now both producers were modeled to deliver against a bottomhole pressure of 10^6 Pa with productivity index of 4×10^{-12} m^3. The potential differences between the injector and the two producers can be seen in Figure 17.

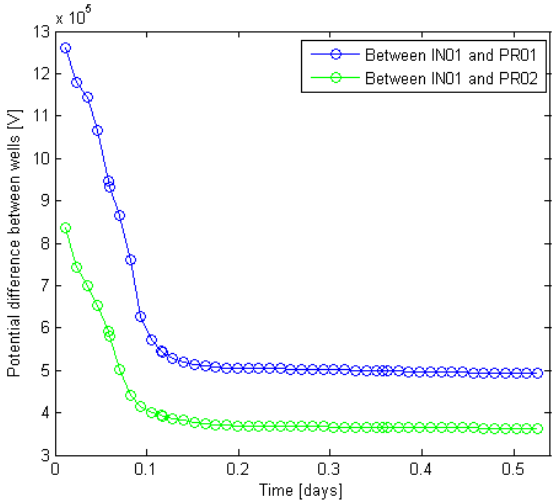

Figure 17: Time histories of potential differences between for Case 4.

The potential difference drops faster between injector IN01 and producer PR02 as expected because they are located closer to each other than IN01 and PR01. The shape of the curves are different from the curves in Figure 16 since the tracer is now being distributed through the network towards two production wells instead of one. The potential difference drops until after around 0.12 days when the tracer has reached both wells and thereby gone through all possible fractures towards the producers.

If the tracer flow is examined, see Figure 18, it can be seen that after 0.08 days when the tracer has reached the production well, both the left and the right paths of the fracture network have been formed with tracer for the electric current to go through.

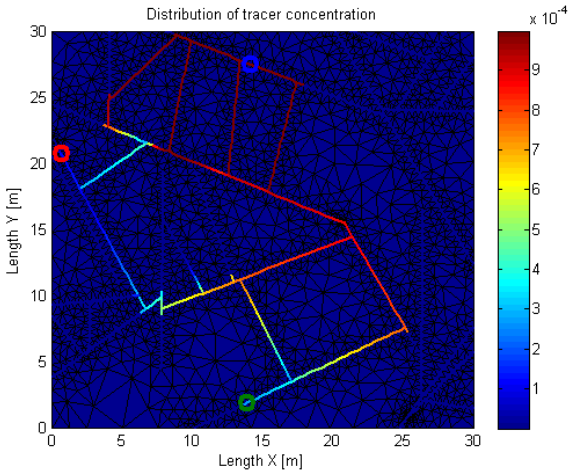

Figure 18: Tracer distribution in the reservoir for Case 4 after 0.08 days of tracer injection.

The potential difference will therefore keep dropping until both paths are fully concentrated with tracer

instead of dropping until the first path is fully concentrated and then stop dropping until the second path is concentrated with tracer, as in Case 1. Figure 19 shows the potential difference for Case 4 compared to Case 1.

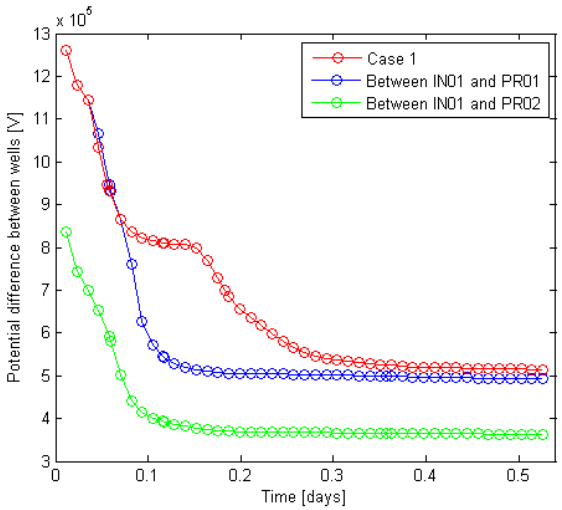

Figure 19: Time histories of potential differences for Case 1 and Case 4.

As mentioned previously, in Case 1 the current goes only through the right fracture path of the reservoir, which has the lowest resistance, until the tracer has reached through the whole left path. Therefore, the potential difference in Case 1 stops dropping once the fractures on the right part of the reservoir are fully concentrated with tracer and until the producer has gotten some tracer from the left path as well. In Case 4, the difference is that once the tracer has reached the right path it has also reached the left path, so instead of stop dropping the potential difference keeps going down until both paths are fully concentrated with tracer.

CONCLUSION

The EOS9 module in TOUGH2 was used to calculate the electric field for two simple fracture networks as tracer was being injected into the reservoirs. The results showed that the history of the potential difference between an injector and a producer was dependent on the fracture network. Four cases where the fractures were modeled using a Discrete Fracture Network (DFN) approach were studied as well. The curve of potential difference between wells was dependent on the fracture network and the well locations and dropped fast as soon as the tracer reached the production well.

These examples were useful to explore the relationship between the potential differences and fracture patterns and to thereby gain better insight into how the time history of the potential difference can be used to indicate some fracture characteristics. Different fracture patterns need to be studied to further understand that relationship but we ran into trouble when using the DFN code for other networks. Egill and Horne (2010) concluded that the problem is likely to be related to the time stepping algorithm and/or that the solvers used by TOUGH2 are not capable of solving the complex equations. Therefore, using the Stanford General Purpose Reservoir Simulator (GPRS) (Cao, 2002; Voskov, 2006) as they did instead of TOUGH2 might be necessary.

FUTURE WORK

Future work includes looking at more fracture networks and greater number of wells to study further the relationship between fracture networks and the change in potential differences as conductive tracer is injected into the reservoir. Future work also includes implementing self-potential calculations into the model since the change in self-potential affects the measured potential difference and could facilitate fracture characterization.

Other future goals are to use tracer concentration simulations and electrical potential calculations from TOUGH2 with inverse modeling to estimate the dimensions and topology of a fracture network. The objective is to develop a method which can be used to find where fractures are located and to characterize their distribution.

ACKNOWLEDGEMENT

This research was supported by the US Department of Energy, under Contract DE-FG36-08GO18192. The Stanford Geothermal Program is grateful for this support.

REFERENCES

Cao, H.: Development of techniques for general purpose simulators, Ph.D. Thesis, Stanford University, Stanford, CA (2002).

Holder, D.S.: Electrical Impedance Tomography: Methods, History and Applications, IOP, UK (2004).

Juliusson, E, and Horne, R.N.: Fracture Characterization using Production and Injection Data, *DOE Quarterly Report (2009 January to March), Contract DE-FG36-08GO18182*, (2009), 1-17.

Juliusson, E, and Horne, R.N.: Study and Simulation of Tracer and Thermal Transport in Fractured Reservoirs, *Proceedings*, 35th Workshop on

Geothermal Reservoir Engineering, Stanford University, Stanford, CA (2010).

Karimi-Fard, M., Durlofsky, L.J. and Aziz, K.: An Efficient Discrete Fracture Model Applicable for General Purpose Reservoir Simulators, SPE 79699, SPE Reservoir Simulation Symposium, Houston, TX (2003).

Magnusdottir, L. and Horne, R.: Characterization of Fractures in Geothermal Reservoirs using Resistivity, *Proceedings*, 36th Workshop on Geothermal Reservoir Engineering Stanford University, Stanford, CA (2011).

Muskat, M.: Potential Distributions in Large Cylindrical Disks with Partially Penetrating Electrodes, *Physics*, **2**, (1932), 329-364.

Pritchett, J.W.: Finding Hidden Geothermal Resources in the Basin and Range Using Electrical Survey Techniques. A Computational Feasibility Study (2004).

Shewchuk J.R.: Triangle: Engineering a 2D Quality; Mesh Generator and Delaunay Triangulator, *Applied Computational Geometry: Towards Geometric Engineering*, **1148**, (1996), 203-222.

Singha, K. and Gorelick, S.M. Saline Tracer Visualized with Three-dimensional Electrical Resistivity Tomography: Field-scale Spatial Moment Analysis. *Water Resources Research*, **41,** (2005), W05023.

Slater, L., Binley, A.M., Daily, W. and Johnson, R. Cross-hole Electrical Imaging of a Controlled Saline Tracer Injection. *Journal of Applied Geophysics*, **44**, (2000), 85-102.

Ucok, H., Ershaghi, I. and Olhoeft, G.R.: Electrical Resistivity of Geothermal Brines, *Journal of Petroleum Technology*, **32**, (1980), 717-727.

Voskov, D.: Description of the Thermal GPRS, Technical Report, Department of Energy Resources Engineering, Stanford University, Stanford, CA (2006).